

# ESTIMATION OF SPATIAL RESOLUTION FOR 3-LAYER J-PET SCANNER USING TOF FBP BASED ON EVENT-BY-EVENT APPROACH\*

R.Y. SHOPA

for the J-PET Collaboration

Department of Complex Systems, National Centre for Nuclear Research  
05-400 Otwock-Świerk, Poland

*(Received November 25, 2019)*

We define a modified time-of-flight (TOF) filtered back projection (FBP) image reconstruction method, proposed for the Jagiellonian PET (J-PET) scanners of high temporal resolution. It is shown that TOF FBP could be represented as a sum of single-event reconstructions, each performed within a small volume in image space around the most likely position (MLP) of positronium annihilation, using TOF and filtering kernels. Such an approach, which resembles spherically-symmetric kernel density estimation (KDE), is highly scalable with the perspective of being employed for real time imaging. Using GATE (Geant4 Application for Tomographic Emission), we simulated the experiment conducted earlier for 1-mm spherical source put inside 3-layer 50-cm long J-PET prototype, eventually comparing the results. Estimated transverse spatial resolution of about 5–8 mm was achieved using TOF FBP for both simulations and real data, which is similar or better than obtained by KDE and non-TOF FBP from STIR software package. Axial resolution of  $\sim 20$  mm was estimated for the simulations using all reconstruction methods, which is consistent with temporal properties of tube photomultipliers utilised for the readout. Substantially worse result ( $\sim 35$  mm in axial direction for TOF FBP), obtained for the experiment, could be explained by unoptimised setup, data pre-selection and/or calibration issues.

DOI:10.5506/APhysPolB.51.181

## 1. Introduction

The developments in time-of-flight (TOF) positron emission tomography (PET) drastically expand the field of study regarding image reconstruction techniques. Today, there are plenty of scintillation crystals, available to

---

\* Presented at the 3<sup>rd</sup> Jagiellonian Symposium on Fundamental and Applied Subatomic Physics, Kraków, Poland, June 23–28, 2019.

achieve coincidence resolving time (CRT) of  $\sim 100$  ps [1–3], such as cerium-doped lutetium oxyorthosilicate (LSO:Ce), lutetium–yttrium oxyorthosilicate (LYSO:Ce) and lanthanum bromide ( $\text{LaBr}_3\text{:Ce}$ ) [4–6]. In reality, the highest temporal resolution, announced by Siemens for their Biograph Vision scanner [7], is only 214 ps, while the other modern clinical TOF-scanners have CRT of about 250–400 ps [8–11].

A distinct approach, introduced in novel total-body Jagiellonian PET (J-PET) scanners, might result in even higher CRT resolution. The detection principle is based on the Compton scattering of (back-to-back) 511 keV  $\gamma$ -quanta inside plastic scintillation strips [12–19], which are superior to traditional PET crystals time-wise [20–23]. TOF information is available *ab initio*: optical signals, generated by each scattering, propagate through the strip in opposite directions and are registered as time tags by photomultipliers (PMTs) [24]. The main drawback of these compounds is low scintillation efficiency, which may be compensated by the application of multi-layer detector with long axial field-of-view (FOV) [12, 25]. Besides, TOF-based algorithms produce outstanding results for much lower statistics compared to non-TOF and even outperform iterative methods at lower CRT (see the discussion in [26]). On the other hand, multi-layer J-PET geometry and elongated strips might require unique approaches in image reconstruction, unavailable in present software solutions.

Filtered back projection (FBP) is one of the oldest PET reconstruction algorithms [27], now used as a reference method and a standard for the estimation of spatial resolution [28]. 3D version of FBP is based on the aggregation of multiple filtered 2D projections (sinograms) [29] and, in theory, could be represented as a sum of 3D reconstructions of separate events, each defined by a single line-of-response (LOR). TOF allows to estimate the most likely position (MLP) of electron–positron or positronium [30, 31] annihilation, therefore, the truncation of the LOR can be considered far from the MLP. The ultimate volume of non-zero intensity (called region-of-response — ROR) is defined by CRT-related uncertainties along Cartesian axes and expected to be much smaller than the FOV of the scanner. This idea was successfully implemented for real-time ROR reconstruction in J-PET by the programmable logic and visualization by the integrated processors [14], yet without the FBP. In this paper, we extend this idea to the algorithm of TOF FBP image reconstruction, applied in event-by-event way.

## 2. Methods

### 2.1. Time-of-flight modification of filtered back projection

For the conventional FBP, the projection data  $p(s, \phi, \zeta, \theta)$  is defined by four variables — transaxial coordinates  $s$  and  $\phi$ ,  $z$ -coordinate of the centre

of the LOR  $\zeta$  and the obliqueness angle  $\theta$  [29] (Fig. 1). The filtering is made in Fourier space using 1-dimensional function  $W(\nu_s)$  of the frequency coordinate  $\nu_s$  associated with  $s$

$$p^F(s, \phi, \zeta, \theta) = \mathcal{F}^{-1} \{W(\nu_s)\mathcal{F}[p(s, \phi, \zeta, \theta)]\}, \quad (1)$$

where  $\mathcal{F}$  and  $\mathcal{F}^{-1}$  are Fourier and inverse Fourier transform operators, respectively. TOF could be added as a Gaussian temporal kernel  $h(t - t_i)$  for  $i^{\text{th}}$  TOF bin [32], expanding the dimensionality of projections to  $\mathbb{R}^5$ . It might as well reflect each separate LOR, represented by the difference of the detection times for back-to-back  $\gamma$ -quanta  $t_i = t_2^{(i)} - t_1^{(i)} (i = 1 \dots N_{\text{LOR}})$ . The unique filtered projection element will be defined as

$$p_i^F \equiv p_i^F(s, \phi, \zeta, \theta, t) = \mathcal{F}^{-1} \{W(\nu_s)\mathcal{F}[p_i(s, \phi, \zeta, \theta)]\} h(t - t_i), \quad (2)$$

where  $p_i(s, \phi, \zeta, \theta)$  is delta-like function, since  $i$  denotes LOR index

$$p_i(s, \phi, \zeta, \theta) = \begin{cases} 1, & s = s_i \cap \phi = \phi_i \cap \zeta = \zeta_i \cap \theta = \theta_i, \\ 0, & \text{otherwise.} \end{cases} \quad (3)$$

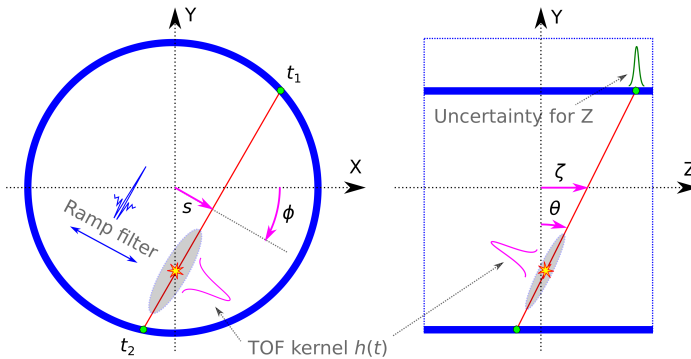


Fig. 1. Schematic depiction of one annihilation event (detection times  $t_1$  and  $t_2$ ) inside cylindrical J-PET scanner for transverse ( $XY$ ) and axial ( $YZ$ ) views. Grey ellipses denote truncated ROR around the annihilation point, defined from three kernels:  $h(t)$ , uncertainty of hit position (detection) along  $Z$  and ramp filter.

The dimensionality of  $p_i^F$  thus will be reduced to  $\mathbb{R}^2$  as three variables will be fixed to  $\phi_i, \zeta_i$  and  $\theta_i$ . Moreover, filtering of unnormalised unit impulse from Eq. (3) in projection space will return the filter  $w(s) = \mathcal{F}^{-1}W(\nu_s)$  itself:  $p_i(s) * w(s) = w(s)$ . The reconstructed image  $f(\mathbf{v})$  will be, therefore,

composed of single-LOR back-projections

$$f(\mathbf{v}) = \sum_{i=1}^{N_{\text{LOR}}} f_i(\mathbf{v}) = \sum_{i=1}^{N_{\text{LOR}}} \mathcal{B} \{p_i^{\text{F}}(s, \phi_i, \zeta_i, \theta_i, t)\}. \quad (4)$$

Despite each voxel  $\mathbf{v}$  could be rigorously evaluated from the variables in projection space  $(s, \phi, \zeta, \theta, t)$ , it is evident from (2) and (3) that each back-projection  $\mathcal{B}\{p_i^{\text{F}}\}$  is merely two kernels, applied to  $i^{\text{th}}$  event:  $h(t)$ -related Gaussian along a LOR and  $w(s)$  — in perpendicular direction. Using MLPs of annihilations, these functions can be redefined in image space. For real scanner, third (Gaussian) kernel should be imposed along  $Z$  due to uncertainty of axial hit position (Fig. 1).

There is no need to recalculate  $f(\mathbf{v})$  over the whole FOV for each event: most voxels have zero or close to zero intensity. At the specific distance from the annihilation point (MLP), a truncation could be applied (see [33]) limiting the ROR to an ellipsoid with the largest axis of few centimetres only (grey areas in Fig. 1). We explored that the reasonable span for the normal distributions imposed along LOR and  $Z$  with standard deviations  $\sigma_{\text{TOF}}$  and  $\sigma_Z$ , respectively, corresponds to at least  $\pm 3.5\sigma$ .  $\sigma_Z$  could be derived from the voxel size,  $\sigma_{\text{TOF}} = c_0 \text{CRT}/(4\sqrt{2\log 2})$ ,  $c_0$  denotes the speed of light. For *apodised ramp filter* — the default choice of  $W(\nu_s)$  for FBP — the truncation could be set at  $\pm 9.0\Delta s$ , where  $\Delta s$  is the sampling interval for  $s$  variable.

## 2.2. Simulation and experiment

According to the National Electrical Manufacturers Association (NEMA) standard [28], the measurements of a point-like radioactive source placed at six different positions inside PET scanner must be conducted for the analysis of spatial resolution. Although not being the best solution, FBP is required to ensure that the true intrinsic properties of the scanner are preserved.

Using Geant4 Application for Tomographic Emission (GATE) framework [34, 35], we performed simulations of such NEMA sources (1-mm spheres of activity 370 kBq) placed inside the second-generation J-PET prototype [24]: 3-cylindrical layers of radii of 42.5 cm, 46.75 cm and 57.5 cm, comprising 48, 48 and 96 scintillation strips, respectively, each of the size of 7 mm  $\times$  19 mm  $\times$  500 mm (Fig. 2, left). Separate simulations were run for each position of the source,  $10^5$  coincidences per each, for three locations in transverse plane ( $x_{\text{src}} = 1$  cm, 10 cm and 20 cm,  $y_{\text{src}} = 0$  cm) and two — for axial coordinate:  $z_{\text{src}} = 0$  cm (the centre of the axial FOV) and  $z_{\text{src}} = 18.75$  cm (three-eighths of the axial FOV — see details in [36]). Hit times  $t_1$  and  $t_2$ , as well as axial positions of hits were smeared according to the resolution CRT = 314 ps, measured experimentally for tube PMs (PMT) utilised for the readout [25].

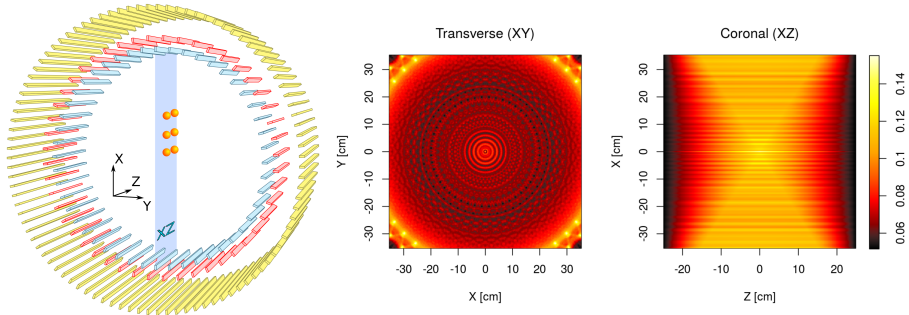


Fig. 2. 3-layer J-PET prototype (left) and its sensitivity map in transverse ( $z = 0$  cm) and coronal ( $y = 0$  cm) cross sections (right). Positions of NEMA sources, defined for the simulation, are depicted on  $XZ$ -plane (left, radii of the sources are exaggerated).

For comparison, we took the real data from an early experiment conducted inside the mentioned 3-layer J-PET prototype, using  $^{22}\text{Na}$  spherical sources with different activities [37]. Only a subset of  $1.5 \times 10^5$  events from each measurement were used, despite much larger statistics (over  $10^6$ ), obtained by 3-hour run for each setup. The sources were fixed on a prepared styrofoam panel at  $x_{\text{src}} = 0$  cm,  $y_{\text{src}} = 1$  cm/10 cm/20 cm,  $z_{\text{src}} = 0$  cm/ $-18.75$  cm (for details, see [37]).

Sparse character of 3-layer J-PET requires the sensitivity map  $s(\mathbf{v})$  to be used for the correction of the reconstructed image:  $f_{\text{corrected}}(\mathbf{v}) = f(\mathbf{v})/s(\mathbf{v})$ . It was generated using hybrid method from [38], mixing two 2D sensitivity maps for axial and transverse planes, obtained analytically and using Monte Carlo simulation, respectively (see Fig. 2, right).

### 2.3. Reference algorithms

#### 2.3.1. Software for Tomographic Image Reconstruction

As a reference point, we employed non-TOF 3D FBP, implemented in popular Software for Tomographic Image Reconstruction (STIR) [39] with the embedded SAFIR module [40] (transforms input data from the list-mode into a suitable Interfile format) and 3D re-projection (3DRP) of Kinahan and Rogers [41] (reduces the truncation problem at edges of the scanner). Unfortunately, STIR does not support multilayer geometry and continuous detectors, therefore, the data had to be pre-processed for FBP 3DRP. Moving along LORs, we remapped all scattering points onto a virtual ideal 1-layer cylindrical scanner (radius  $R = 43.73$  cm, 384 strips of the same size as in real prototype, divided axially to form 96 discrete “rings”, each 0.52-cm wide). Times and axial coordinates of hits were adjusted correspondingly. No sensitivity map was applied afterwards.

### 2.3.2. Multivariate kernel density estimation

The proposed TOF FBP is in fact kernel-based approach, hence it is reasonable to compare it with multivariate kernel density estimation (KDE), applied directly to MLP of annihilation points, estimated from TOF. For a dataset of MLPs  $\{\mathbf{X}_1, \mathbf{X}_2, \dots, \mathbf{X}_n\}$  of a size  $n$ , KDE is defined as

$$\hat{f}_{n\mathbf{H}}(\mathbf{x}) = n^{-1} \sum_{i=1}^n |\mathbf{H}|^{-1/2} \mathcal{K} \left[ \mathbf{H}^{-1/2} (\mathbf{x} - \mathbf{X}_i) \right], \quad (5)$$

where  $\mathbf{x} \equiv \mathbf{v} = (x, y, z)^T$ ,  $\mathbf{H}$  is the bandwidth matrix, symmetric and positive definite [42]. Spherically symmetric kernel  $\mathcal{K}(\cdot)$  can be defined as Gaussian or other function, but its choice is not critical for a large  $n$ , unlike  $\mathbf{H}$  — a covariance matrix that controls the amount and orientation of smoothing induced. We employed built-in estimators for  $\mathbf{H}$  from popular R package 'ks' [43]: `samse` (based on asymptotic approximation mean integrated squared error) and `dscalar` (multistage plug-in bandwidth selector) [42]. Unlike FBP, the employed KDE/MLP method does not apply filtering on transverse plane, but the optimisation of  $\mathbf{H}$  may improve axial resolution.

## 3. Results and discussion

Point spread function (PSF) was analysed from transverse ( $XY$ ) and axial ( $XZ$  or  $YZ$ ) cross sections of the reconstructed images cut along the voxel of the highest intensity. Due to a relatively large voxel size ( $\Delta x \times \Delta y \times \Delta z = 1.8 \text{ mm} \times 1.8 \text{ mm} \times 2.6 \text{ mm}$  for TOF FBP and FBP 3DRP), the spatial resolution, estimated as FWHM (full width at half maximum), was calculated with the accuracy of 0.5 mm for all axis.

Transverse and axial cross sections of the reconstructed images for the selected positions of the source are presented in Fig. 3 for all utilised algorithms, both for the simulations and experimental data. In general, the latter produces worse results in terms of spatial resolution, which poorly correlates with the projected properties of the scanner. This could be explained by the imperfect pre-selection of the data, calibration issues of PMTs and readout electronics, as well as bootstrapping the setup for the early experiment [37]. However, despite the need for resolving these problems and new measurements conducted, we could still compare the algorithms.

Estimated PSF values from the simulated data are aggregated into Table I, for two extreme positions — close to the geometrical centre and to the edge of the scanner. As one can see, TOF FBP is consistent with FBP 3DRP, with similar or better outcomes. On the other hand, likewise KDE/MLP, it takes into account the sparse scanner geometry, which could be seen as distorted non-circular shape of the source in transverse plane. The background

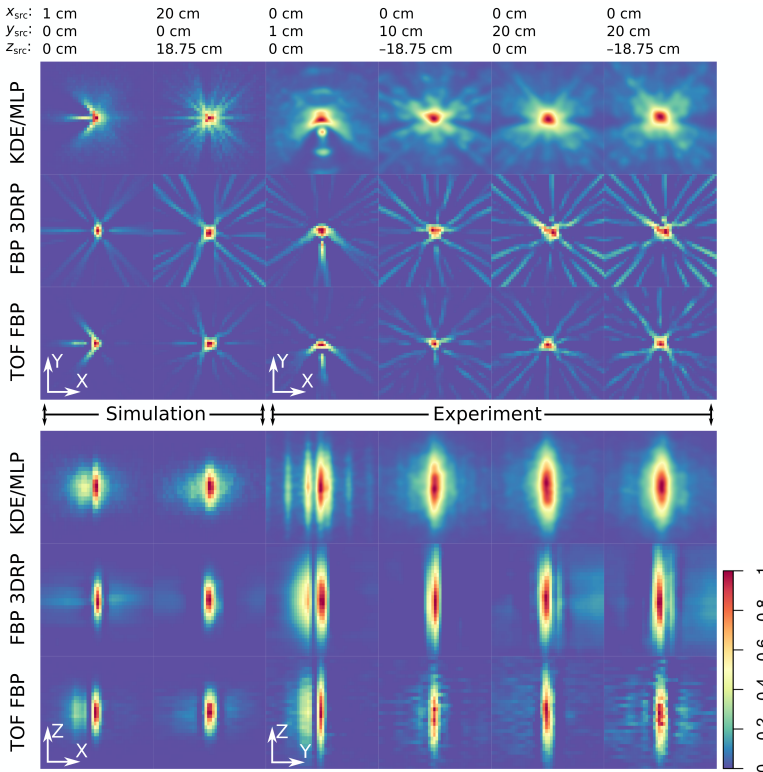


Fig. 3. (Colour on-line) Reconstructed transverse (top) and axial (bottom) cross-sections of 1-mm source placed inside 3-layer J-PET scanner at selected locations ( $x_{src}$ ,  $y_{src}$ ,  $z_{src}$ ), performed using three algorithms: KDE/MLP, FBP 3DRP (from STIR) and TOF FBP. The regions shown are of  $8\text{ cm} \times 8\text{ cm}$  size each, centred at the projected coordinates of the source (denoted on top), set for GATE simulations (first two columns) and experimental measurements (last four columns).

noise is the lowest for TOF FBP and the highest for KDE/MLP, as expected, which was confirmed by the analysis of full width at tenth maximum, defined by NEMA [28].

For the data gained from real measurements, the remapping of hits onto a virtual single layer, required by STIR, affects significantly the result, since, unlike for GATE simulations, the exact  $XY$ -positions of scatterings inside the strip are unavailable. This imposes additional blur in transverse plane, therefore, the current application of FBP 3DRP from STIR framework is inferior to TOF FBP, as seen from the images (last four columns in Fig. 3).

Estimated FWHM values for all six positions of the source that represent spatial resolution are depicted in Fig. 4. TOF FBP evidently produces the most consistent results between the simulation and the experiment in

TABLE I

Selected PSF values, estimated from the reconstructions of the simulated 1-mm point source, located at  $(x_{\text{src}}, y_{\text{src}}, z_{\text{src}})$  in J-PET scanner.

| Source position<br>( $y_{\text{src}} = 0$ cm) | Algorithm<br>applied | Resolution [mm] |     |      |
|---|----------------------|-----------------|-----|------|
|   |                      | X               | Y   | Z    |
| $x_{\text{src}} = 1$ cm                       | KDE/MLP              | 5.5             | 6.0 | 20.0 |
| $z_{\text{src}} = 0$ cm<br>(centre)           | FBP 3DRP             | 4.5             | 7.0 | 20.0 |
|   | TOF FBP              | 5.0             | 6.5 | 20.5 |
| $x_{\text{src}} = 20$ cm                      | KDE/MLP              | 7.5             | 6.0 | 22.0 |
| $z_{\text{src}} = 18.75$ cm<br>(edge)         | FBP 3DRP             | 6.5             | 7.5 | 21.0 |
|   | TOF FBP              | 7.0             | 5.5 | 18.0 |

transverse plane. KDE/MLP, though being the worst for  $XY$ , appears to be the best in axial direction. This outcome underlines the importance of the optimisation of bandwidth matrix  $\mathbf{H}$ , which was calculated using plug-in selector method from [42]. On the other hand, the parameters of Gaussian kernels, employed for TOF FBP ( $\sigma_{\text{TOF}}$  and  $\sigma_Z$  — see Eq. (2) and Fig. 1), would worsen the resolution if set too wide. We explored that three-fold decrease of  $\sigma_{\text{TOF}}$  that narrows  $h(t)$  reduces additional axial smearing to minimum. However, it also adds noise, clearly visible in Fig. 3 (last row), hence a proper optimisation is required for the kernels used in TOF FBP, similar to bandwidth selection approach from KDE.

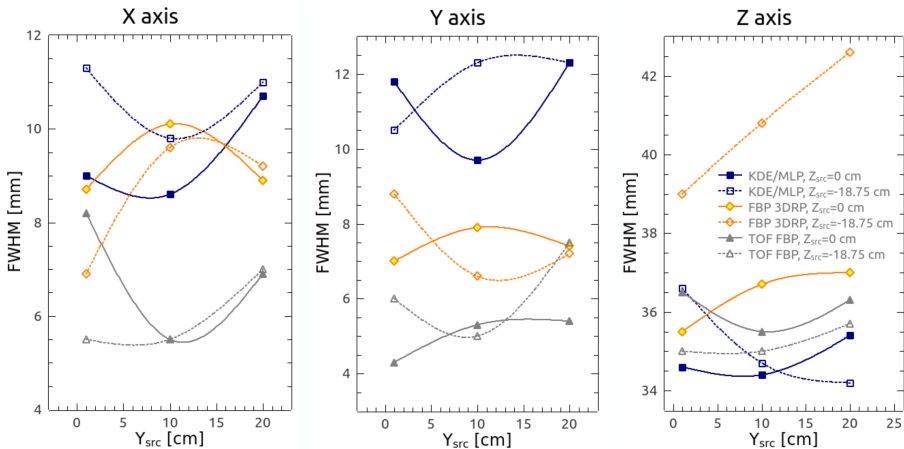


Fig. 4. Estimated spatial resolution (FWHM) of 3-layer J-PET scanner, calculated from experimental data, reconstructed by KDE/MLP, FBP 3DRP and TOF FBP.

#### 4. Conclusion

The proposed implementation of TOF FBP algorithm, applied to the reconstruction of a point-like source, exhibits promising results, similar or better than conventional FBP. Operated directly in image space as asymmetrical 3D kernel, this solution is capable of processing separate events in parallel, which opens up a possibility for the application in real time imaging. Estimated transverse spatial resolution of 5–8 mm (both for simulations and real measurements) is consistent with the geometry of 3-layer J-PET scanner prototype. TOF information also improves axial resolution, even for the simplest KDE/MLP method. However, further experiments are required for the validation of the estimated PSF<sub>Z</sub> ~ 20 mm, obtained for the simulated data, because the result for the measurements appeared to be worse by 75% and does not reflect PMT timing properties. Moreover, there is a need for the rigorous optimisation of TOF FBP kernels — standard deviations of Gaussian functions ( $\sigma_{\text{TOF}}$  and  $\sigma_Z$ ) and apodisation window set for ramp filter. Such procedure would differ from bandwidth selection, approved for KDE, since the latter is acceptable only for spherically symmetrical kernels.

We acknowledge the financial support of the Polish National Centre for Research and Development through grant INNOTECH-K1/IN1/64/159174/NCBR/12, the Foundation for Polish Science through MPD and TEAM POIR.04.04.00-00-4204/17 programmes, the National Science Centre, Poland (NCN) through grant Nos. 2016/21/ B/ST2/01222, 2017/25/N/NZ1/00861, the Ministry for Science and Higher Education through grant Nos. 6673/IA/SP/2016, 7150/E-338/SPUB/2017/1, the EU and MSHE grant No. POIG.02.03.00-161 00-013/09.

#### REFERENCES

- [1] D. Schaart *et al.*, *Phys. Med. Biol.* **55**, N179 (2010).
- [2] S. Gundacker *et al.*, *JINST* **8**, P07014 (2013).
- [3] M. Nemallapudi *et al.*, *Phys. Med. Biol.* **60**, 4635 (2015).
- [4] C. Melcher *et al.*, *IEEE Trans. Nucl. Sci.* **39**, 502 (1992).
- [5] W.W. Moses *et al.*, *IEEE Trans. Nucl. Sci.* **46**, 474 (1999).
- [6] A. Kuhn *et al.*, *IEEE Trans. Nucl. Sci.* **51**, 2550 (2004).
- [7] J. van Sluis *et al.*, *J. Nucl. Med.* **60**, 1031 (2019).
- [8] S. Surti *et al.*, *J. Nucl. Med.* **48**, 471 (2007).
- [9] S. Vandenberghe *et al.*, *EJNMMI Phys.* **3**, 3 (2016).
- [10] A.M. Grant *et al.*, *Med. Phys.* **43**, 2334 (2016).

- [11] J.S. Karp *et al.*, to be printed in *J. Nucl. Med.*, 2019, available on-line: DOI:10.2967/jnumed.119.229997.
- [12] P. Moskal *et al.*, *Phys. Med. Biol.* **61**, 2025 (2016).
- [13] L. Raczyński *et al.*, *Phys. Med. Biol.* **62**, 5076 (2017).
- [14] G. Korcyl *et al.*, *IEEE Trans. Med. Im.* **37**, 2526 (2018).
- [15] M. Pałka *et al.*, *JINST* **12**, P08001 (2017).
- [16] P. Moskal *et al.*, *Nucl. Instrum. Methods Phys. Res. A* **764**, 317 (2014).
- [17] P. Moskal *et al.*, *Nucl. Instrum. Methods Phys. Res. A* **775**, 54 (2015).
- [18] L. Raczyński *et al.*, *Nucl. Instrum. Methods Phys. Res. A* **764**, 186 (2014).
- [19] L. Raczyński *et al.*, *Nucl. Instrum. Methods Phys. Res. A* **786**, 105 (2015).
- [20] M. Conti, *Phys. Med.* **25**, 1 (2009).
- [21] J.L. Humm *et al.*, *Eur. J. Nucl. Med. Mol. Imaging* **30**, 1574 (2003).
- [22] J.S. Karp *et al.*, *J. Nucl. Med.* **49**, 462 (2008).
- [23] D.W. Townsend, *Ann. Acad. Med. Singapore* **33**, 133 (2004).
- [24] S. Niedźwiecki *et al.*, *Acta Phys. Pol. B* **48**, 1567 (2017).
- [25] P. Kowalski *et al.*, *Phys. Med. Biol.* **63**, 165008 (2018).
- [26] V. Westerwoudt *et al.*, *IEEE Trans. Nucl. Sci.* **61**, 126 (2014).
- [27] S. Helgason, *Groups and Geometric Analysis. Integral Geometry, Invariant Differential Operators and Spherical Functions*, Academic Press, Orlando 1984, p. 654.
- [28] National Electrical Manufacturers Association, Norm NEMA-NU-2, 2012.
- [29] D.L. Bailey, D.W. Townsend, P.E. Valk, M.N. Maisey, *Positron Emission Tomography, Basic Sciences*, Springer, London 2005, p. 382.
- [30] P. Moskal *et al.*, *Phys. Med. Biol.* **64**, 055017 (2019).
- [31] P. Moskal *et al.*, *Nature Rev. Phys.* **1**, 527 (2019).
- [32] M. Conti *et al.*, *Phys. Med. Biol.* **50**, 4507 (2005).
- [33] N. Efthimiou *et al.*, *Phys. Med. Biol.* **64**, 035004 (2019).
- [34] S. Jan *et al.*, *Phys. Med. Biol.* **49**, 4543 (2004).
- [35] S. Jan *et al.*, *Phys. Med. Biol.* **56**, 881 (2011).
- [36] R.Y. Shopa *et al.*, *Acta Phys. Pol. B* **48**, 1757 (2017).
- [37] M. Pawlik-Niedźwiecka *et al.*, *Acta Phys. Pol. A* **132**, 1645 (2017).
- [38] A. Strzelecki, Image reconstruction and simulation of strip positron emission tomography scanner using computational accelerators, Ph.D. Thesis, Institute of Fundamental Technological Research, Polish Academy of Sciences, Kraków 2016.
- [39] K. Thielemans *et al.*, *Phys. Med. Biol.* **57**, 867 (2012).
- [40] R. Becker *et al.*, *Nucl. Instrum. Methods Phys. Res. A* **845**, 648 (2017).
- [41] P. Kinahan *et al.*, *IEEE Trans. Nucl. Sci.* **36**, 964 (1990).
- [42] J.E. Chacón *et al.*, *Test* **19**, 375 (2010).
- [43] T. Duong, *J. Stat. Soft.* **21**, 1 (2007).